

Target search of active agents crossing high energy barriers

Luigi Zanovello,^{1,2} Michele Caraglio,¹ Thomas Franosch,^{1,*} and Pietro Faccioli^{2,3,†}

¹*Institut für Theoretische Physik, Universität Innsbruck,
Technikerstraße 21A, A-6020, Innsbruck, Austria*

²*Dipartimento di Fisica, Università degli studi di Trento, Via Sommarive 14, 38123 Trento, Italy*

³*INFN-TIFPA, Via Sommarive 14, 38123 Trento, Italy*

(Dated: January 14, 2021)

Target search by active agents in rugged energy landscapes has remained a challenge because standard enhanced sampling methods do not apply to irreversible dynamics. We overcome this non-equilibrium rare-event problem by developing an algorithm generalizing transition-path sampling to active Brownian dynamics. This method is exemplified and benchmarked for a paradigmatic two-dimensional potential with a high barrier. We find that even in such a simple landscape the structure and kinetics of the ensemble of transition paths changes drastically in the presence of activity. Indeed, active Brownian particles reach the target more frequently than passive Brownian particles, following longer and counterintuitive search patterns.

Active matter and directed motion are receiving increasing attention because of their relevance in a wide range of research fields, including biology, biomedicine, robotics, and statistical physics [1, 2]. Active propulsion allows bacteria and animals to explore their local environment and forage nutrients [1, 3] and is key to the development of new nanoparticles that may act as drug delivery agents [4–7]. Furthermore, phagocytes of the immune system perform chemotactic motion during injury or infection [8, 9] and sperm cells navigate against chemical gradients to find the egg [10]. The central question in all these examples is how active agents find their target. In spite of its relevance, to date this problem has been addressed by relatively few theoretical studies. In particular, only the special case of run-and-tumble motion [11] was investigated within the framework of intermittent search patterns [12–16].

Target search crucially depends on the environment [11], and in many realistic scenarios it involves exploring a complex energy landscape, characterized by the presence of several local minima, separated by energy barriers. Unfortunately, the computational cost of simulating the dynamics by directly integrating the equations of motions grows exponentially with the ruggedness of the landscape and the height of the barriers.

For passive systems, similar problems have been solved by the development of enhanced sampling methods [6, 17–22, 24–27] but much less attention has been devoted to enhanced sampling applications on active particles, with the notable exceptions of a case study of alignment interactions in a modified Vicsek model [28] and of systems displaying motility-induced phase separation [29, 30]. Among the various enhanced sampling algorithms, transition-path sampling (TPS) [20–22] has the advantage to provide a completely rigorous sampling of the reactive trajectories between a reactant basin and a target basin. This algorithm is essentially a Metropolis Monte Carlo performed in the space of reactive trajectories. Trial moves are generated by choosing a random

state on a known reactive path and integrating the equations of motion (shooting) forward and backward in time to obtain a new transition path. Trial moves are then accepted or rejected according to some probability explicitly calculated from the equations of motion. The main problem encountered when applying TPS to active target search concerns the possibility to apply backward shooting. In passive systems, this is possible, because the backward probability is directly related to forward dynamics by microscopic reversibility. The dynamics of a self-propelled particle, however, is microscopically irreversible, therefore it is commonly believed that backward shooting is not allowed. To overcome this problem, other methods such as forward flux sampling (FFS) [26, 27] have been specifically developed to account also for non-equilibrium systems. Nevertheless, these methods suffer other limitations, such as an efficiency drop due to the impossibility to shoot backward in time and the need to know *a priori* a proper reaction coordinate, which could be not always possible on complex energy landscapes. Recently, two novel methods [28] addressed this challenge by bridging between the original TPS and the FFS methodology. As TPS, they aim at importance sampling of trajectory space and are independent of the choice of a reaction coordinate. Yet, as FFS, they allow only forward shooting and may therefore be inefficient in certain situations.

Here, we show for the first time that in the case of an active Brownian particle (ABP) the lack of microscopic reversibility can be circumvented and backward shooting may therefore become feasible. The result is a generalized version of the original TPS algorithm, in which the acceptance probability contains a new term depending explicitly on the particle’s activity. We then apply our new scheme to study how the activity affects target search in a two-dimensional landscape, characterized by the presence of a large energy barrier.

We first consider an ensemble of microswimmers initially confined to some reactant region R , searching for

some target region T. A single microswimmer is modeled as an ABP in two dimensions, i.e. the equations of motion consist of a set of Langevin equations in which the activity is provided by a stochastic drive proportional to a velocity term of modulus v and subject to a rotational diffusion process. If the ABP diffuses in a conservative energy landscape $U(x, y)$, the equations of motion discretized according to the Itô rule are

$$\mathbf{r}_{i+1} = \mathbf{r}_i + v \mathbf{u}_i \Delta t - \mu \nabla U(\mathbf{r}_i) \Delta t + \sqrt{2D\Delta t} \boldsymbol{\xi}_i, \quad (1)$$

$$\vartheta_{i+1} = \vartheta_i + \sqrt{2D_\vartheta \Delta t} \eta_i, \quad (2)$$

where Δt is the integration step, $\mathbf{r}_i = (x_i, y_i)$ is the position at time $i\Delta t$ and $\mathbf{u}_i = (\cos \vartheta_i, \sin \vartheta_i)$ denotes the instantaneous orientation of the driving velocity. D and D_ϑ are the translational and rotational diffusion coefficients, respectively, and μ is an effective mobility [31]. Finally, the components of the vector noise $\boldsymbol{\xi}_i = (\xi_{x,i}, \xi_{y,i})$ and of the scalar noise η_i are independent random variables, distributed according to a Gaussian with zero average and unit variance. In the following we refer to the microstate of a single active particle as $w = (\vartheta, \mathbf{r})$.

To sample the reactive paths from R to T we reconsider the TPS algorithm [21, 22] and adapt it to the present case of ABPs. In TPS, a Markov chain of reactive trajectories is generated starting from some arbitrary initial path. Trial moves (newly attempted transition paths \mathcal{W}^{new} generated starting from an old path \mathcal{W}^{old}) are proposed according to a three-step procedure: First, a microstate w_i^{old} is randomly picked from the frames in \mathcal{W}^{old} . Next, the microstate may be modified by means of some random perturbation: $w_i^{\text{old}} \rightarrow w_j^{\text{new}}$. Finally, a new trial trajectory \mathcal{W}^{new} is obtained by shooting forward and backward in time, starting from w_j^{new} (see Supplemental Material [32] – SM). The resulting new trajectory \mathcal{W}^{new} is then accepted with a probability \mathcal{P}_{acc} , which is calculated from the underlying microscopic dynamics by imposing the detailed balance condition in the functional space of reactive trajectories. This results in a standard Metropolis rule

$$\mathcal{P}_{\text{acc}} [\mathcal{W}^{\text{old}} \rightarrow \mathcal{W}^{\text{new}}] = h[\mathcal{W}^{\text{new}}] \times \min \left\{ 1, \frac{\mathcal{P}[\mathcal{W}^{\text{new}}] \mathcal{P}_{\text{gen}}[\mathcal{W}^{\text{new}} \rightarrow \mathcal{W}^{\text{old}}]}{\mathcal{P}[\mathcal{W}^{\text{old}}] \mathcal{P}_{\text{gen}}[\mathcal{W}^{\text{old}} \rightarrow \mathcal{W}^{\text{new}}]} \right\}, \quad (3)$$

where $h[\mathcal{W}^{\text{new}}]$ is a characteristic function equal to one only if the new path is reactive and zero otherwise. $\mathcal{P}[\mathcal{W}]$ is the functional path probability density which reads

$$\mathcal{P}[\mathcal{W}] \propto \rho(w_0) \prod_{i=0}^{N-1} p(w_i \rightarrow w_{i+1}), \quad (4)$$

where N is the number of frames of the reactive path \mathcal{W} , and $\rho(w_0)$ is the quasi-stationary non-equilibrium distri-

bution of initial conditions in the reactant. Further,

$$p(w_i \rightarrow w_{i+1}) \propto \exp \left\{ -\frac{(\vartheta_{i+1} - \vartheta_i)^2}{4D_\vartheta \Delta t} \right\} \times \exp \left\{ -\frac{(\mathbf{r}_{i+1} - \mathbf{r}_i - v \mathbf{u}_i \Delta t + \mu \nabla U(\mathbf{r}_i) \Delta t)^2}{4D\Delta t} \right\}, \quad (5)$$

is the conditional probability for performing a transition from w_i to w_{i+1} in the infinitesimal time interval Δt as is readily derived from Eq. (1) (see SM). $\mathcal{P}_{\text{gen}}[\mathcal{W}]$ in Eq. (3) is the probability of generating a trial path, according to the shooting procedure outlined above. Explicitly,

$$\mathcal{P}_{\text{gen}}[\mathcal{W}^\alpha \rightarrow \mathcal{W}^\beta] = \mathcal{P}_{\text{sel}}(w_j^\alpha | \mathcal{W}^\alpha) \mathcal{P}_{\text{pert}}(w_j^\alpha \rightarrow w_i^\beta) \times \prod_{k=i}^{N^\beta-1} p(w_k^\beta \rightarrow w_{k+1}^\beta) \prod_{k=0}^{i-1} \bar{p}(w_{k+1}^\beta \rightarrow w_k^\beta), \quad (6)$$

where $\mathcal{P}_{\text{sel}}(w_j^\alpha | \mathcal{W}^\alpha) = 1/N^\alpha$ is the probability of selecting as shooting point the state w_j^α belonging to the reactive path \mathcal{W}^α of length N^α . $\mathcal{P}_{\text{pert}}(w_j^\alpha \rightarrow w_i^\beta)$ is the probability of perturbing w_j^α to obtain the microstate w_i^β of the path \mathcal{W}^β of length N^β [38, 39]. The first and second product of probabilities in the second line of Eq. (6) represent the probability of generating the two branches of the trial trajectory \mathcal{W}^β connecting the microstate w_i^β to the target and reactant state, respectively. In particular, $\bar{p}(w_{i+1} \rightarrow w_i)$ is the probability to observe a transition from the microstate w_{i+1} to the microstate w_i in a dynamics evolving backwards in time. For passive Brownian dynamics, this backward probability is directly related to the forward one by microscopic reversibility. However, the dynamics of ABPs is intrinsically irreversible [40] and the calculation of $\bar{p}(w_{i+1} \rightarrow w_i)$ is non-trivial. In principle, one could use any sort of backward dynamics, and consistently derive the corresponding acceptance probability within the TPS approach by following the procedure explained below. However, the challenge is to find moves that are efficient in sampling the reactive paths, which is possible if the trial moves have a significant overlap with the “real dynamics”. Here we suggest for the backwards shooting the simple rule:

$$\begin{aligned} \mathbf{r}_i &= \mathbf{r}_{i+1} - v \mathbf{u}_{i+1} \Delta t - \mu \nabla U(\mathbf{r}_{i+1}) \Delta t + \sqrt{2D\Delta t} \boldsymbol{\xi}_{i+1}, \\ \vartheta_i &= \vartheta_{i+1} + \sqrt{2D_\vartheta \Delta t} \eta_{i+1}. \end{aligned} \quad (7)$$

Note that Eq. (S9) is formally equivalent to Eq. (1) but with a flipped sign of the driving velocity, treating this term as odd under time-reversal symmetry [3]. Furthermore, the sign of the potential gradient term guarantees that in the limit $v \rightarrow 0$ Eq. (S9) reduces to the correct backward dynamics of a passive Brownian particle (see SM for details). From these equations, it is possible to obtain an analytic expression of the backward-transition

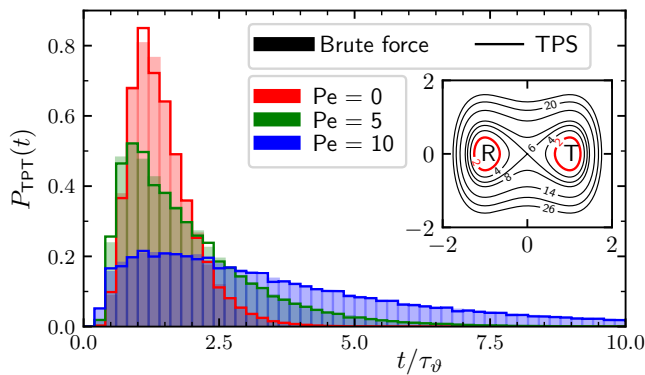


FIG. 1. Distribution of Transition-path times (TPTs) at different Péclet numbers. Each distribution is obtained from 10^6 different TPTs. ($\tau_\vartheta = 1/D_\vartheta$)

probability (see SM for details)

$$\bar{p}(w_{i+1} \rightarrow w_i) = p(w_i \rightarrow w_{i+1}) \frac{\pi(\mathbf{r}_i)}{\pi(\mathbf{r}_{i+1})} \times \frac{\exp\left\{-\frac{v}{2D}\mathbf{u}_{i+1} \cdot (\mathbf{r}_i - \mathbf{r}_{i+1} + \mu\nabla U(\mathbf{r}_{i+1})\Delta t)\right\}}{\exp\left\{-\frac{v}{2D}\mathbf{u}_i \cdot (\mathbf{r}_i - \mathbf{r}_{i+1} - \mu\nabla U(\mathbf{r}_i)\Delta t)\right\}}, \quad (9)$$

where $\pi(\mathbf{r}) \propto e^{-\beta U(\mathbf{r})}$ is the Boltzmann distribution for a passive particle. We stress that the first line of Eq. (S6) is the result for a passive Brownian particle, while the second line represents the correction term accounting for the microscopic irreversibility of active Brownian dynamics. Similar results expressing the ratio between the forward and backward probability may be obtained by a direct time-reversal transformation within the path integral formulation [41] or by means of Crooks-like relations for entropy production [42], in a similar fashion to what has been done in different contexts [40, 43, 44].

After combining all terms, the final expression for the acceptance probability can be obtained. This formula is rather lengthy and can be found in SM. Here we limit ourselves to noting that in the limit of vanishing activity ($v \rightarrow 0$) we recover the standard TPS formula for passive Brownian dynamics. We also stress that the acceptance probability involves the steady-state distribution of microstates in the reactant basin $\rho(w)$, which is in general not known analytically. We numerically estimated this distribution from a frequency histogram of the microstates in the reactant basin visited by active Brownian trajectories generated by solving numerically Eq. (1) (see SM).

We use our TPS algorithm to characterize transition pathways of an ABP reaching a target region crossing the energy barrier in the two-dimensional energy surface

$$U(x, y) = k_x(x^2 - x_0^2)^2 + \frac{k_y}{2}y^2, \quad (10)$$

which provides the paradigmatic example of a double well problem. We set $x_0 = 1$, $k_x = 6$ and $k_y = 20$ and

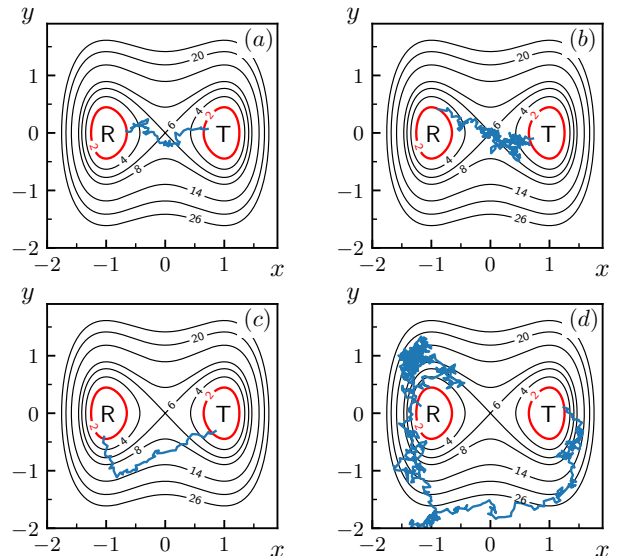


FIG. 2. (a-b) A fast and a slow reactive path ($t_{\text{TPT}}/\tau_\vartheta = 0.65$ and 2.37 respectively) of a passive Brownian particle ($\text{Pe} = 0$). The red contour lines are the borders of the R and T basins. (c-d) A fast and a slow reactive path ($t_{\text{TPT}}/\tau_\vartheta = 0.53$ and 8.36 respectively) of an ABP ($\text{Pe} = 10$).

measure energy in units of an effective thermal energy $k_B T_{\text{eff}} := D/\mu$. We define a reactive trajectory as one leaving the reactant region (defined as the set of points with $U(x, y) \leq 2k_B T_{\text{eff}}$ and $x < 0$) and reaching the target region (defined by $U(x, y) \leq 2k_B T_{\text{eff}}$ and $x > 0$), before returning to the reactant. Here we study the ABP behavior for three different values of the Péclet number, $\text{Pe} := v\sqrt{3/4DD_\vartheta}$, a dimensionless measure of the activity: $\text{Pe} = 0$ ($v = 0$), $\text{Pe} = 5$ ($v = 1.83$) and $\text{Pe} = 10$ ($v = 3.65$) while keeping fixed $D = 0.1$, $D_\vartheta = 1$ and $\mu = 0.1$. Important insight on the ABPs behavior in a potential well has already been achieved, for example the escape rates do not follow Kramers theory [45, 46] and they depend explicitly on the full potential barrier [5]. Here we first consider the distribution of transition-path times (TPTs), i.e. the time durations of reactive trajectories. This observable has received considerable attention in the context of passive dynamics, both from experimentalists [48–51] and theorists [52–61], because it carries information about the reactive dynamics. Yet, it appears that TPTs in the presence of activity have been studied only in the case of a one-dimensional particle crossing a parabolic barrier [62].

The TPT distribution obtained using our TPS algorithm reproduces well the one obtained by direct integration of the stochastic equations of motion (see Fig. 1) for the different values of the Péclet number. The computational advantage of sampling by TPS relative to brute force simulations is very high at low activities but drops significantly at very large activities. In the present landscape, the ratio between the time needed to obtain 10^6

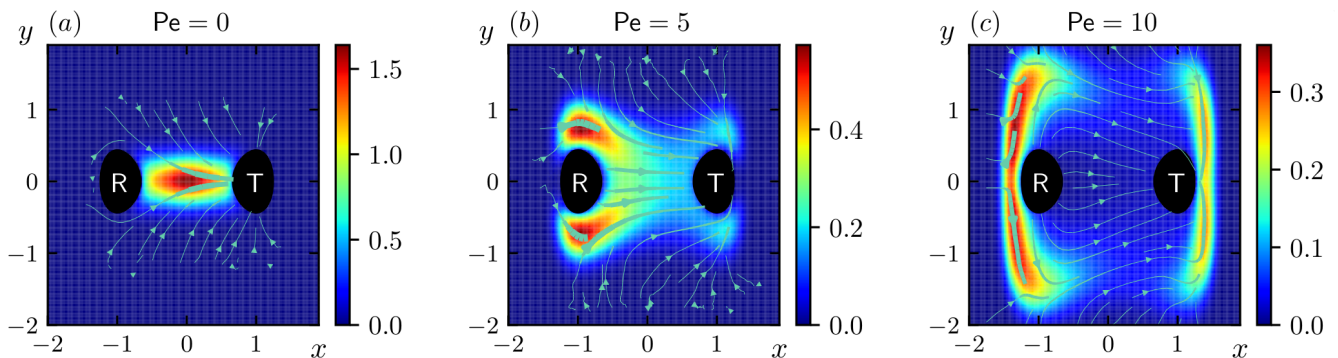


FIG. 3. (a-c) Reactive probability density $m(\mathbf{r})$ (color map) and field lines of the reactive current $\mathbf{J}(\mathbf{r})$ (cyan arrows) at different Péclet numbers.

reactive paths with TPS and brute force simulations is ~ 0.001 , ~ 0.12 and ~ 0.27 for $Pe = 0$, $Pe = 5$ and $Pe = 10$, respectively. This decrease in efficiency strictly follows the increase with the activity of crossing rates (see SM) and we expect that the computational advantage of TPS for active particles increases for larger barriers. Note that, if the TPS scheme is modified accordingly, these results are also confirmed when a different backward dynamics is adopted. However, this could strongly affect the algorithm's efficiency (see section IV in SM).

Our results show that the average TPT grows with the Péclet number, while the distribution becomes broader and broader. To investigate the origin of this difference, it is instructive to analyze the typical transition pathways. For a passive particle the slow and fast trajectories are quite similar, with the reactive paths narrowly focused around the minimum-energy path crossing the barrier (see Fig. 2 a-b). In contrast, for active particles the trajectories associated with fast and slow transitions are qualitatively very different. Namely, fast active transition pathways are similar to passive ones (see Fig. 2c). In contrast, the main contribution to the right tail of the TPT distribution comes from trajectories which leave the reactant basin in the direction opposite to energy saddle point (see Fig. 2d) [63].

This mechanism is confirmed by a systematic statistical analysis of the reactive processes, based on computing the transition-path density, $m(\mathbf{r})$, and the transition current, $\mathbf{J}(\mathbf{r})$ [64]. Here $m(\mathbf{r})$ measures the probability that a transition path visits a specific position \mathbf{r} in the reactive region, while $\mathbf{J}(\mathbf{r})$ provides the information on the probability current. At vanishing Pe the transition-path density is highest in the saddle point region, while upon adding activity the transition-path density becomes largest in the regions behind the basins, as shown in Fig. 3. This behavior is reflected in the reactive current (see Fig. 3) as well as in the marginalized reactive probability density $m(x) = \int m(x, y) dy$ and $m(y) = \int m(x, y) dx$ (see SM).

Altogether, our results demonstrate that active target search is qualitatively different from that performed by

passive systems. In particular, the observed two order of magnitude increase of the target-finding rates due to the self-propulsion (see SM) is concomitant with the observation that the ABPs reach the target by exploring regions of the energy landscape that are effectively inaccessible for the passive particle. While one could still naively expect that also for ABPs most of the reactive paths are rather short and develop close to the minimum energy path, we show that long-lasting paths become more and more frequent with increasing activity. Moreover, in contrast to the passive case, the structure of the transition pathways of active particles qualitatively changes as a function of its TPT: while short trajectories travel along the minimum energy path (in qualitative analogy with the passive case), long-lasting trajectories reach the target in a counter-intuitive way, by climbing the energy surface in the direction opposite to the transition state and then “surfing” high energy regions in the potential energy landscape, before landing into the target. Overall, this picture is confirmed also when considering other energy landscapes and different set of parameters (see SM). Interestingly, the average TPT increases with the activity of the particle while the opposite behavior is observed in one-dimensional systems [62]. Yet, there the reactive pathways reaching the target from the back cannot even occur, correspondingly the observed trend underlines the non-trivial interplay arising between the activity of the particle, the dimensionality of the system, and the environment topology.

In summary, we have addressed the problem of characterizing the structure and kinetics of rare transition pathways undergone by ABPs in search for a target. To this end, we have derived and validated an extension of TPS which can be used to directly sample rare events undergone by ABPs. For the first time we have shown that the explicit breaking of microscopic reversibility typical of non-equilibrium systems does not prevent from exploiting backward dynamics in order to develop an efficient TPS algorithm. Using our TPS algorithm, we have compared the behavior of active and passive Brownian particles reaching a target in a two-dimensional energy

landscape characterized by a high energy barrier.

Our results show that, far from equilibrium conditions, significant differences emerge between the reactive kinetics of active and passive particles. ABPs behave as “explorers”: once left the reactant basin it may take longer for them to reach the target but they make many more successful attempts and do that by visiting a large portion of the surrounding space. In contrast, the passive particles are more “creatures of habit”: they like to stay in their basin and when moving to the target they are very quick and always follow the same path. We expect similar counter-intuitive target search patterns to be found in a wide range of physical systems of biological, chemical, and technological relevance and the enhanced path sampling scheme developed in this work provides a powerful tool to investigate these processes in a computationally efficient way.

The mathematical scheme we adopted to derive the acceptance rule for ABPs may in principle be applied to a wider class of irreversible systems, as long as it is possible to identify a backward dynamics with a well-defined path probability density and as long as the trajectories obtained by joining the backward and the forward segments remain “smooth” (i.e. they look like the trajectories obtained with only forward dynamics). Straightforward examples include chiral ABPs [65], active particles with anisotropic diffusion [66], and active Ornstein-Uhlenbeck particles [67, 68]. Possibly, one could deal also with particles that orient themselves along spatial gradients [69] by including a bias term in Eq. (2) and leaving untouched Eq. (1-S9-S10) but this, as well every other possible choice, should be verified by checking the feasibility and efficiency of the resulting TPS scheme. Finally, the idea that backward shooting is possible also when there is a lack of microscopic reversibility may have applications going beyond TPS, as conceiving new enhanced sampling algorithms or generalizing existing ones.

We thank Peter G. Bolhuis, Oleksandr Chepizhko, and Hartmut Löwen for useful discussions. This work was supported by the Austrian Science Fund (FWF): P28687-N27.

* Thomas.Franosch@uibk.ac.at

† pietro.faccioli@unitn.it

- [1] C. Bechinger, R. Di Leonardo, H. Löwen, C. Reichhardt, G. Volpe, and G. Volpe, Active particles in complex and crowded environments, *Rev. Mod. Phys.* **88**, 045006 (2016).
- [2] M. C. Marchetti, J. F. Joanny, S. Ramaswamy, T. B. Liverpool, J. Prost, M. Rao, and R. A. Simha, Hydrodynamics of soft active matter, *Rev. Mod. Phys.* **85**, 1143 (2013).
- [3] J. Elgeti, R. Winkler, and G. G., Physics of microswimmers—single particle motion and collective behavior: a review, *Rep. Prog. Phys.* **78**, 056601 (2015).
- [4] S. Naahidi, M. Jafari, F. Edalat, K. Raymond, A. Khademhosseini, and P. Chen, Biocompatibility of engineered nanoparticles for drug delivery, *J. Control. Rel.* **166**, 182 (2013).
- [5] D. Patra, S. Sengupta, W. Duan, H. Zhang, R. Pavlick, and A. Sen, Intelligent, self-powered, drug delivery systems, *Nanoscale* **5**, 1273 (2013).
- [6] U. Kei Cheang, K. Lee, A. A. Julius, and M. J. Kim, Multiple-robot drug delivery strategy through coordinated teams of microswimmers, *Appl. Phys. Lett.* **105**, 083705 (2014).
- [7] J. Liu, T. Wei, J. Zhao, Y. Huang, H. Deng, A. Kumar, C. Wang, Z. Liang, X. Ma, and X.-J. Liang, Multifunctional aptamer-based nanoparticles for targeted drug delivery to circumvent cancer resistance, *Biomaterials* **91**, 44 (2016).
- [8] P. N. Devreotes and S. H. Zigmond, Chemotaxis in eukaryotic cells: A focus on leukocytes and dictyostelium, *Annu. Rev. Cell Biol.* **4**, 649 (1988).
- [9] S. de Oliveira, E. E. Rosowski, and A. Huttenlocher, Neutrophil migration in infection and wound repair: going forward in reverse, *Nat. Rev. Immunol.* **16**, 378 (2016).
- [10] M. Eisenbach and L. C. Giojalas, Sperm guidance in mammals – an unpaved road to the egg, *Nat. Rev. Mol. Cell Biol.* **7**, 276 (2006).
- [11] G. Volpe and G. Volpe, The topography of the environment alters the optimal search strategy for active particles, *Proc. Natl. Acad. Sci. USA* **114**, 11350 (2017).
- [12] O. Bénichou, C. Loverdo, M. Moreau, and R. Voituriez, Intermittent search strategies, *Rev. Mod. Phys.* **83**, 81 (2011).
- [13] G. M. Viswanathan, S. V. Buldyrev, S. Havlin, M. G. E. da Luz, E. P. Raposo, and H. E. Stanley, Optimizing the success of random searches, *Nature* **401**, 911 (1999).
- [14] O. Bénichou, M. Coppey, M. Moreau, P.-H. Suet, and R. Voituriez, Optimal search strategies for hidden targets, *Phys. Rev. Lett.* **94**, 198101 (2005).
- [15] O. Bénichou, C. Loverdo, M. Moreau, and R. Voituriez, Two-dimensional intermittent search processes: An alternative to Lévy flight strategies, *Phys. Rev. E* **74**, 020102 (2006).
- [16] G. Viswanathan, E. Raposo, and M. da Luz, Lévy flights and superdiffusion in the context of biological encounters and random searches, *Phys. Life Rev.* **5**, 133 (2008).
- [17] G. Torrie and J. J.P. Valleau, Nonphysical sampling distributions in Monte Carlo free-energy estimation: Umbrella sampling, *J. Comput. Phys.* **23**, 187 (1977).
- [18] A. Laio and M. Parrinello, Escaping free-energy minima, *Proc. Natl. Acad. Sci. USA* **99**, 12562 (2002).
- [19] G. Bowman, V. Pande, and F. Noé, *An Introduction to Markov State Models and Their Application to Long Timescale Molecular Simulation*, Advances in Experimental Medicine and Biology (Springer Netherlands, 2013).
- [20] C. Dellago, P. G. Bolhuis, F. S. Csajka, and D. Chandler, Transition path sampling and the calculation of rate constants, *J. Chem. Phys.* **108**, 1964 (1998).
- [21] P. G. Bolhuis, D. Chandler, C. Dellago, and P. L. Geissler, TRANSITION PATH SAMPLING: Throwing ropes over rough mountain passes, in the dark, *Annu. Rev. Phys. Chem.* **53**, 291 (2002).
- [22] C. Dellago, P. G. Bolhuis, and P. L. Geissler, Transition path sampling, in *Advances in Chemical Physics* (John Wiley & Sons, Ltd, 2003) Chap. 1, pp. 1–78.
- [6] T. S. van Erp, D. Moroni, and P. G. Bolhuis, A novel path sampling method for the calculation of rate constants, *J.*

- Chem. Phys. **118**, 7762 (2003).
- [24] A. K. Faradjian and R. Elber, Computing time scales from reaction coordinates by milestoning, *J. Chem. Phys.* **120**, 10880 (2004).
- [25] J. M. Bello-Rivas and R. Elber, Exact milestoning, *J. Chem. Phys.* **142**, 094102 (2015).
- [26] R. J. Allen, C. Valeriani, and P. R. ten Wolde, Forward flux sampling for rare event simulations, *J. Phys.: Condens. Matter* **21**, 463102 (2009).
- [27] S. Hussain and A. Haji-Akbari, Studying rare events using forward-flux sampling: Recent breakthroughs and future outlook, *J. Chem. Phys.* **152**, 060901 (2020).
- [28] P. Buijsman and P. G. Bolhuis, Transition path sampling for non-equilibrium dynamics without predefined reaction coordinates, *J. Chem. Phys.* **152**, 044108 (2020).
- [29] G. S. Redner, C. G. Wagner, A. Baskaran, and M. F. Hagan, Classical nucleation theory description of active colloid assembly, *Phys. Rev. Lett.* **117**, 148002 (2016).
- [30] S. Whitelam, Sampling rare fluctuations of discrete-time Markov chains, *Phys. Rev. E* **97**, 032122 (2018).
- [31] For a passive particle the mobility is related to the translational diffusion coefficient via the fluctuation-dissipation theorem $D = \mu k_B T$, with T the temperature of the thermal bath in which the particle is immersed.
- [32] See Supplemental Material at [URL] for details on stochastic path integral, acceptance probability, steady states, more discussion for $Pe = 5$, and additional figures. The Supplemental Material includes Refs. [33-37].
- [1] L. Onsager and S. Machlup, Fluctuations and irreversible processes, *Phys. Rev.* **91**, 1505 (1953).
- [2] S. Machlup and L. Onsager, Fluctuations and irreversible process. II. Systems with kinetic energy, *Phys. Rev.* **91**, 1512 (1953).
- [3] S. Shankar and M. C. Marchetti, Hidden entropy production and work fluctuations in an ideal active gas, *Phys. Rev. E* **98**, 020604 (2018).
- [4] C. Dellago, P. G. Bolhuis, and D. Chandler, Efficient transition path sampling: Application to Lennard-Jones cluster rearrangements, *J. Chem. Phys.* **108**, 9236 (1998).
- [7] T. S. van Erp and P. G. Bolhuis, Elaborating transition interface sampling methods, *J. Comput. Phys.* **205**, 157 (2005).
- [38] Note that the two paths \mathcal{W}^α and \mathcal{W}^β in general have different lengths and that consequently the index i is unlikely to be equal to index j .
- [39] Due to the stochastic nature of its dynamics, for an ABP the perturbation of the shooting point is not necessary. Hence, we set $w_i^\beta = w_j^\alpha$ with probability equal to one.
- [40] L. Dabelow, S. Bo, and R. Eichhorn, Irreversibility in active matter systems: Fluctuation theorem and mutual information, *Phys. Rev. X* **9**, 021009 (2019).
- [41] G. Falasco, R. Pfaller, A. P. Bregulla, F. Cichos, and K. Kroy, Exact symmetries in the velocity fluctuations of a hot Brownian swimmer, *Phys. Rev. E* **94**, 030602 (2016).
- [42] G. E. Crooks, On thermodynamic and microscopic reversibility, *J. Stat. Mech. Theor. Exp.* **2011**, P07008 (2011).
- [43] T. Speck, Stochastic thermodynamics for active matter, *Europhys. Lett.* **114**, 30006 (2016).
- [44] D. Chaudhuri, Active Brownian particles: Entropy production and fluctuation response, *Phys. Rev. E* **90**, 022131 (2014).
- [45] A. Geiseler, P. Hänggi, and G. Schmid, Kramers escape of a self-propelled particle, *Eur. Phys. J. B* **89**, 175 (2016).
- [46] P. Romanczuk, M. Bär, W. Ebeling, B. Lindner, and L. Schimansky-Geier, Active Brownian particles, *Eur. Phys. J. Special Topics* **202**, 1 (2012).
- [5] E. Woillez, Y. Zhao, Y. Kafri, V. Lecomte, and J. Tailleur, Activated escape of a self-propelled particle from a metastable state, *Phys. Rev. Lett.* **122**, 258001 (2019).
- [48] H. S. Chung, J. M. Louis, and W. A. Eaton, Experimental determination of upper bound for transition path times in protein folding from single-molecule photon-by-photon trajectories, *Proc. Natl. Acad. Sci. USA* **106**, 11837 (2009).
- [49] K. Neupane, D. A. N. Foster, D. R. Dee, H. Yu, F. Wang, and M. T. Woodside, Direct observation of transition paths during the folding of proteins and nucleic acids, *Science* **352**, 239 (2016).
- [50] K. Neupane, F. Wang, and M. T. Woodside, Direct measurement of sequence-dependent transition path times and conformational diffusion in DNA duplex formation, *Proc. Natl. Acad. Sci. USA* **114**, 1329 (2017).
- [51] K. Neupane, N. Q. Hoffer, and M. T. Woodside, Measuring the local velocity along transition paths during the folding of single biological molecules, *Phys. Rev. Lett.* **121**, 018102 (2018).
- [52] M. Sega, P. Faccioli, F. Pederiva, G. Garberoglio, and H. Orland, Quantitative protein dynamics from dominant folding pathways, *Phys. Rev. Lett.* **99**, 118102 (2007).
- [53] B. W. Zhang, D. Jasnow, and D. M. Zuckerman, Transition-event durations in one-dimensional activated processes, *J. Chem. Phys.* **126**, 074504 (2007).
- [54] P. Faccioli and F. Pederiva, Microscopically computing free-energy profiles and transition path time of rare macromolecular transitions, *Phys. Rev. E* **86**, 061916 (2012).
- [55] W. K. Kim and R. R. Netz, The mean shape of transition and first-passage paths, *J. Chem. Phys.* **143**, 224108 (2015).
- [56] D. E. Makarov, Shapes of dominant transition paths from single-molecule force spectroscopy, *J. Chem. Phys.* **143**, 194103 (2015).
- [57] M. Laleman, E. Carlon, and H. Orland, Transition path time distributions, *J. Chem. Phys.* **147**, 214103 (2017).
- [58] A. M. Berezhkovskii, L. Dagdug, and S. M. Bezrukov, Mean direct-transit and looping times as functions of the potential shape, *J. Phys. Chem. B* **121**, 5455 (2017).
- [59] M. Caraglio, S. Put, E. Carlon, and C. Vanderzande, The influence of absorbing boundary conditions on the transition path time statistics, *Phys. Chem. Chem. Phys.* **20**, 25676 (2018).
- [60] A. M. Berezhkovskii, L. Dagdug, and S. M. Bezrukov, Exact solutions for distributions of first-passage, direct-transit, and looping times in symmetric cusp potential barriers and wells, *J. Phys. Chem. B* **123**, 3786 (2019).
- [61] M. Caraglio, T. Sakaue, and E. Carlon, Transition path times in asymmetric barriers, *Phys. Chem. Chem. Phys.* **22**, 3512 (2020).
- [62] E. Carlon, H. Orland, T. Sakaue, and C. Vanderzande, Effect of memory and active forces on transition path time distributions, *J. Phys. Chem. B* **122**, 11186 (2018).
- [63] Clearly, it takes a time of the order of the rotational diffusion time before the particle points again in a favorable direction, thus leading to long TPTs.
- [64] W. E and E. Vanden-Eijnden, Transition-path theory and path-finding algorithms for the study of rare events, *Annu. Rev. Phys. Chem.* **61**, 391 (2010).
- [65] S. van Teeffelen and H. Löwen, Dynamics of a Brownian

- circle swimmer, *Phys. Rev. E* **78**, 020101 (2008).
- [66] C. Kurzthaler, S. Leitmann, and T. Franosch, Intermediate scattering function of an anisotropic active Brownian particle, *Sci. Rep.* **6**, 36702 (2016).
- [67] L. L. Bonilla, Active Ornstein-Uhlenbeck particles, *Phys. Rev. E* **100**, 022601 (2019).
- [68] L. Caprini, U. Marini Bettolo Marconi, A. Puglisi, and A. Vulpiani, Active escape dynamics: The effect of persistence on barrier crossing, *J. Chem. Phys.* **150**, 024902 (2019).
- [69] O. Pohl and H. Stark, Dynamic clustering and chemotactic collapse of self-phoretic active particles, *Phys. Rev. Lett.* **112**, 238303 (2014).

**Supplemental Material for
'Target search of active agents crossing high energy barriers'**

Luigi Zanovello^{1,2}, Michele Caraglio¹, Thomas Franosch¹, and Pietro Faccioli^{2,3}

¹ *Institut für Theoretische Physik, Universität Innsbruck, Technikerstraße 21A, A-6020, Innsbruck, Austria*

² *Dipartimento di Fisica, Università degli studi di Trento, Via Sommarive 14, 38123 Trento, Italy*

³ *INFN-TIFPA, Via Sommarive 14, 38123 Trento, Italy*

**STOCHASTIC PATH INTEGRAL FOR ACTIVE PARTICLES AND DERIVATION OF THE
BACKWARD PROBABILITY**

Here we provide the derivation of the forward transition probability in a discrete dynamics as in Eq. (1-2) of the main text together with its path integral formulation. We also derive the backward transition probability.

Considering equations of motion of the ABP –Eq. (1-2) in the main text–, and that the components of the vector noise $\xi_i = (\xi_{x,i}, \xi_{y,i})$ and of the scalar noise η_i are independent random variables, distributed according to a Gaussian with zero average and unit variance, one can readily write down the probability for a transition between two microstates:

$$\begin{aligned} p(w_i \rightarrow w_{i+1}) &= \mathcal{N} \exp \left\{ -\frac{(\vartheta_{i+1} - \vartheta_i)^2}{4D_\vartheta \Delta t} \right\} \exp \left\{ -\frac{(\mathbf{r}_{i+1} - \mathbf{r}_i - v\mathbf{u}_i \Delta t + \mu \nabla U(\mathbf{r}_i) \Delta t)^2}{4D \Delta t} \right\} = \\ \mathcal{N}' \exp \left\{ -\frac{(\vartheta_{i+1} - \vartheta_i)^2}{4D_\vartheta \Delta t} \right\} \exp \left\{ -\frac{v^2 \Delta t}{4D} \right\} \exp \left\{ -\frac{v}{2D} \mathbf{u}_i \cdot (\mathbf{r}_i - \mathbf{r}_{i+1} - \mu \nabla U(\mathbf{r}_i) \Delta t) \right\} \pi(\mathbf{r}_i \rightarrow \mathbf{r}_{i+1}), \end{aligned} \quad (\text{S1})$$

where \mathcal{N} and \mathcal{N}' are normalization constants and in the second line we have factorized the probability $\pi(\mathbf{r}_i \rightarrow \mathbf{r}_{i+1})$ for a passive particle going from \mathbf{r}_i to \mathbf{r}_{i+1} in a time step Δt .

Considering that the succession of the states $w_i = (\mathbf{r}_i, \vartheta_i)$ constitutes a Markov process, the probability of finding the system in a specific microstate w_N at time $\tau = N\Delta t$ provided the initial condition w_0 at time $t = 0$ can be obtained as

$$\mathcal{P}(w_N | w_0) = \prod_{i=0}^{N-1} p(w_i \rightarrow w_{i+1}). \quad (\text{S2})$$

The latter, in the limit of $\Delta t \rightarrow 0$, can be rewritten using the following stochastic path integral formulation:

$$\mathcal{P}(w_N | w_0) = \mathcal{Z}^{-1} \int_{\mathbf{r}_0}^{\mathbf{r}_N} \mathcal{D}\mathbf{r} \int \mathcal{D}\vartheta \exp \left(-\frac{1}{4D_\vartheta} S_{\text{rot}}[\vartheta] \right) \exp \left(-\frac{1}{4D} S_{\text{trans}}[\mathbf{r}, \vartheta] \right), \quad (\text{S3})$$

where \mathcal{Z} is again a normalization constant and S_{rot} and S_{trans} are functionals encoding the rotational and translational noise:

$$S_{\text{rot}}[\vartheta] = \int_0^\tau dt \left[\dot{\vartheta}(t) \right]^2, \quad (\text{S4})$$

$$S_{\text{trans}}[\mathbf{r}, \mathbf{u}] = \int_0^\tau dt \left[\dot{\mathbf{r}}(t) - v\mathbf{u}(t) + \mu \nabla U(\mathbf{r}(t)) \right]^2. \quad (\text{S5})$$

Note that S_{trans} is the active equivalent of the Onsager–Machlup functional of a passive particle [S1, S2].

Considering the discrete backward dynamics defined by Eq. (7-8) of the main text and using the same argument that led us to Eq. (S1), the backward transition probability reads

$$\begin{aligned} \bar{p}(w_{i+1} \rightarrow w_i) &= \mathcal{N} \exp \left\{ -\frac{(\vartheta_i - \vartheta_{i+1})^2}{4D_\vartheta \Delta t} \right\} \exp \left\{ -\frac{(\mathbf{r}_i - \mathbf{r}_{i+1} + v\mathbf{u}_{i+1} \Delta t + \mu \nabla U(\mathbf{r}_{i+1}) \Delta t)^2}{4D \Delta t} \right\} = \\ \mathcal{N}' \exp \left\{ -\frac{(\vartheta_i - \vartheta_{i+1})^2}{4D_\vartheta \Delta t} \right\} \exp \left\{ -\frac{v^2 \Delta t}{4D} \right\} \exp \left\{ -\frac{v}{2D} \mathbf{u}_{i+1} \cdot (\mathbf{r}_i - \mathbf{r}_{i+1} + \mu \nabla U(\mathbf{r}_{i+1}) \Delta t) \right\} \pi(\mathbf{r}_{i+1} \rightarrow \mathbf{r}_i), \end{aligned} \quad (\text{S6})$$

which easily leads to Eq. (9) of the main text once one considers that detailed balance condition

$$\pi(\mathbf{r}_{i+1}) \pi(\mathbf{r}_{i+1} \rightarrow \mathbf{r}_i) = \pi(\mathbf{r}_i) \pi(\mathbf{r}_i \rightarrow \mathbf{r}_{i+1}), \quad (\text{S7})$$

holds for a passive particle.

FINAL ACCEPTANCE PROBABILITY

Here we present the final form of the acceptance probability implemented in our generalized TPS algorithm obtained by combining Eq. (3-6,9) of the main paper.

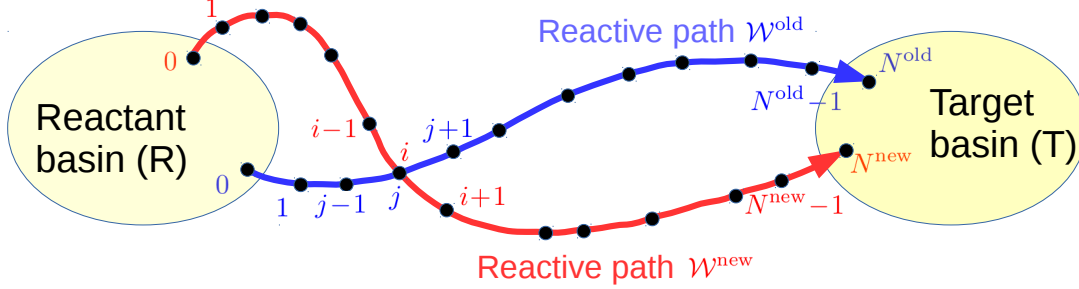


FIG. S1. Sketch representing the TPS algorithm. A new reactive trajectory \mathcal{W}^{new} is generated by solving the system's equations of motion forward and backward in time, starting from $w_j^{\text{new}} = w_i^{\text{old}}$, with w_i^{old} a frame of the old reactive path \mathcal{W}^{old} .

We recall that a newly attempted transition path \mathcal{W}^{new} generated starting from an old path \mathcal{W}^{old} (see Fig. S1) is proposed according to a three-step procedure: First, a microstate w_i^{old} is randomly picked from the frames in \mathcal{W}^{old} . Next, we select as shooting point $w_j^{\text{new}} = w_i^{\text{old}}$. Finally, a new trial trajectory \mathcal{W}^{new} is obtained by solving the system's equations of motion forward and backward in time, starting from w_j^{new} . The resulting new trajectory \mathcal{W}^{new} is then accepted with the following probability

$$\begin{aligned} \mathcal{P}_{\text{acc}}[\mathcal{W}^{\text{old}} \rightarrow \mathcal{W}^{\text{new}}] = h[\mathcal{W}^{\text{new}}] \min \left\{ 1, \frac{N^{\text{old}}}{N^{\text{new}}} \frac{\rho(w_0^{\text{new}})}{\rho(w_0^{\text{old}})} \frac{\pi(\mathbf{r}_0^{\text{old}})}{\pi(\mathbf{r}_0^{\text{new}})} \times \right. \\ \prod_{k=0}^{j-1} \exp \left\{ -\frac{v}{2D} \mathbf{u}_{k+1}^{\text{old}} \cdot (\mathbf{r}_k^{\text{old}} - \mathbf{r}_{k+1}^{\text{old}} + \mu \nabla U(\mathbf{r}_{k+1}^{\text{old}}) \Delta t) \right\} \times \\ \prod_{k=0}^{j-1} \exp \left\{ \frac{v}{2D} \mathbf{u}_k^{\text{old}} \cdot (\mathbf{r}_k^{\text{old}} - \mathbf{r}_{k+1}^{\text{old}} - \mu \nabla U(\mathbf{r}_k^{\text{old}}) \Delta t) \right\} \times \\ \prod_{k=0}^{i-1} \exp \left\{ \frac{v}{2D} \mathbf{u}_{k+1}^{\text{new}} \cdot (\mathbf{r}_k^{\text{new}} - \mathbf{r}_{k+1}^{\text{new}} + \mu \nabla U(\mathbf{r}_{k+1}^{\text{new}}) \Delta t) \right\} \times \\ \left. \prod_{k=0}^{i-1} \exp \left\{ -\frac{v}{2D} \mathbf{u}_k^{\text{new}} \cdot (\mathbf{r}_k^{\text{new}} - \mathbf{r}_{k+1}^{\text{new}} - \mu \nabla U(\mathbf{r}_k^{\text{new}}) \Delta t) \right\} \right\}. \end{aligned} \quad (\text{S8})$$

Note that in the limit of vanishing activity ($v \rightarrow 0$) the previous equation reduces to the standard TPS acceptance probability for passive Brownian dynamics: $\mathcal{P}_{\text{acc}}[\mathcal{W}^{\text{old}} \rightarrow \mathcal{W}^{\text{new}}] = h[\mathcal{W}^{\text{new}}] \min \{1, N^{\text{old}}/N^{\text{new}}\}$.

STEADY STATE DISTRIBUTION WITHIN THE REACTANT BASIN

To implement the TPS algorithm the steady state distribution within the reactant basin is needed. The passive particle is Boltzmann-distributed (see Fig. S2a). In the case of ABP, the steady state distribution is not Boltzmann-distributed and is obtained from a frequency histogram of the microstates in the reactant basin visited by active Brownian trajectories generated by solving numerically Eq. (1-2) of the main text. The resulting distribution shows that when the ABP is inside the reactants basin, it is more likely to be on the left side of the basin (see Fig. S2b). Furthermore, the positional probability distribution of an ABP inside the basin strongly depends on the angle ϑ determining the direction of its velocity (see Fig. S2c-f) The results show that the ABP is more likely to have a velocity that points in the opposite direction with respect to the center of the basin. The observed overall behavior is due to the fact that the left side of the basin is characterized by a steeper potential wall. When the ABP has a

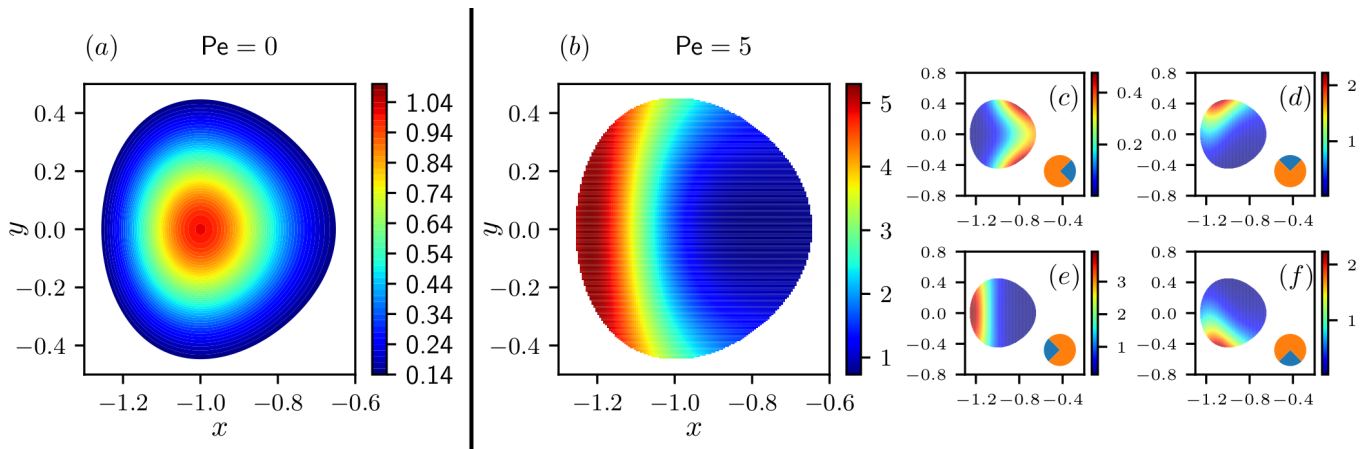


FIG. S2. Steady state distributions within the reactant basin. (a) equilibrium distribution for a passive particle, with $k_x = 6$ and $k_y = 20$. (b) steady state distribution for an active particle with $Pe = 5$, $k_x = 6$ and $k_y = 20$. For each (x, y) point, the distribution value is obtained as the cumulative distribution over all the possible angles ϑ of the self-propulsion speed. (c-f) steady state distribution marginalized on the value of the angle ϑ . The four plot report distributions marginalized on the four quadrant: $-\pi/4 < \vartheta \leq \pi/4$ (c), $\pi/4 < \vartheta \leq 3\pi/4$ (d), $3\pi/4 < \vartheta \leq 5\pi/4$ (e) and $5\pi/4 < \vartheta \leq 7\pi/4$ (f). See also the blue portion in the pie plots.

velocity pointing towards positive x values, it can easily exit the reactant basin. In contrast, when the ABP has a velocity pointing towards the steeper potential wall (direction towards negative x values), it is more likely that the particle remains inside the basin, at least for a time of the order τ_ϑ , which is the typical time necessary for the particle to change the velocity direction.

DEFINITION OF THE BACKWARD DYNAMICS

Here we collect a few remarks about our suggested rule for the backward shooting:

$$\mathbf{r}_i = \mathbf{r}_{i+1} - v \mathbf{u}_{i+1} \Delta t - \mu \nabla U(\mathbf{r}_{i+1}) \Delta t + \sqrt{2D\Delta t} \boldsymbol{\xi}_{i+1}, \quad (\text{S9})$$

$$\vartheta_i = \vartheta_{i+1} + \sqrt{2D_\vartheta \Delta t} \eta_{i+1}, \quad (\text{S10})$$

corresponding to Eq. (7-8) of the main text.

First, we discuss the sign of the self-propulsion term (second term on right side of Eq. (S9)). In order to have trial reactive path (obtained by joining together the backward and forward shoots) resembling as much as possible the reactive paths obtained by integrating the equations of motion only forward in time, the self-propulsion term is treated as odd under time reversal symmetry, i.e. at par with particle momentum, it reverses sign under time reversal. This differs from the even signature in which self propulsion is treated as a non-conservative force and does not change sign under time reversal. See Ref. [S3] for a thorough discussion of the various implication of the choice between the two conventions. However, one is in principle allowed to adopt an even signature convention for the self-propulsion term, provided that Eq. (S6) and Eq. (S8) are modified accordingly. Yet, with this modified scheme it is possible to properly sample the reactive path space only in the presence of a non-negligible contribution of the translational diffusion. This is actually the case for the parameter used to present the results of our manuscript, at the price of an about 10-fold decrease in efficiency. Fig. S3 shows that both schemes using odd signature and even signature reproduce the same TPT distribution.

Second, we discuss the sign of the conservative force term (third term on right side of Eq. (S9)). In this case we opted for a negative sign for the two following reasons:

1. As for the self propulsion term, one is in principle allowed to flip the sign of the force term in the backward dynamics. However, if so the TPS algorithm becomes very inefficient in the sense that new trajectories in the reactive path ensemble are accepted with a very low rate by the Metropolis procedure. Indeed, considering this “flipped sign backward dynamics” and the model parameters reported in the main text, the acceptance rate of new reactive trajectories turns out to be about 4-6 times smaller.

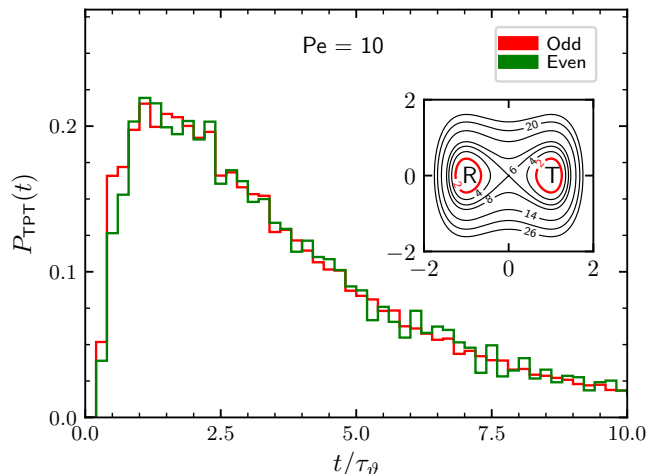


FIG. S3. Comparison of TPT distributions obtained through a TPS scheme in which either odd or even signature of the self-propulsion term in the backward integration step is used (ABP parameters: $D = 0.1$, $v = 3.65$, $\mu = 0.1$, $D_\vartheta = 1$. Potential parameters: $k_x = 6$, $k_y = 20$).

- Our algorithm has the benefit of reducing to the standard equilibrium one for vanishing Péclet number. In the case of passive particles in the overdamped limit the forward and backward probability are indistinguishable (see ref. [22]). In fact, the forward and backward probability are related by microscopic reversibility (see ref. [22]):

$$\pi(\mathbf{r}_i)\pi(\mathbf{r}_i \rightarrow \mathbf{r}_{i+1}) = \pi(\mathbf{r}_{i+1})\bar{\pi}(\mathbf{r}_{i+1} \rightarrow \mathbf{r}_i), \quad (\text{S11})$$

and since detailed balance, Eq. (S7), also holds, it follows that the backward probability is equal to the forward probability

$$\bar{\pi}(\mathbf{r}_{i+1} \rightarrow \mathbf{r}_i) = \pi(\mathbf{r}_{i+1} \rightarrow \mathbf{r}_i), \quad (\text{S12})$$

and that the backward trajectory can be generated using the forward propagation rule.

DETAILED ANALYSIS FOR $Pe = 5$ AND $Pe = 10$

Greater details on the reactive path ensemble can be collected by studying the behavior of the angle ϑ in the states belonging to the transition paths. Here we discuss the case of medium activity $Pe = 5$. Due to symmetry with respect to the axis $y = 0$, the average angle as a function of x is zero. More interestingly, the standard deviation of the angles as a function of x shows that the angles are more focused in forward direction ($\vartheta = 0$) just at the right of the reactants basin (see blue lines Fig. S4b). In fact, the angular distributions of ϑ conditioned to specific values of x are spread around $\vartheta = 0$ at $x = 0$, while they are bimodal in the proximity of the basins (see Fig. S4d). Along the y coordinate, instead, on average the angle points upward for positive y values and downward for negative y values while the standard deviation remains about constant (see Fig. S4c). This behavior is reflected in the angular distributions of ϑ conditioned to specific values of y , as reported in Fig. S4e. Angular distributions conditioned to a specific position show that for points close to the reactant basin the most likely velocity angle points in the direction opposite to the basin itself. However, the angular distribution conditioned to a specific position just above the target basin displays again angles contained in the first quadrant (see Fig. S4 f-g). Altogether, the picture emerging from Fig. S4 is that there are few fast reactive paths similar to the one reported in Fig. 2(c) and many paths similar to the one in Fig. 2(d) (in the main text) that surf along the energy walls before falling in the T basin (see also Fig. S5). Fig. S5 is equivalent to Fig. S4 but in the case of $Pe = 10$.

Different transition pathway are sorted in the three categories by studying their behavior in the region $X : -1 < x < 1$, when going from the R basin to the T basin: Type I) paths whose positions contained in the region X have only positive (or only negative) y values; Type II) paths whose portion contained in the region X has positive (negative) y coordinates when close R and negative (positive) y coordinates when close to T; Type III) other types of trajectories. Fig. S6 reports the frequencies with which different reactive trajectory types are observed. For $Pe = 5$ most of the

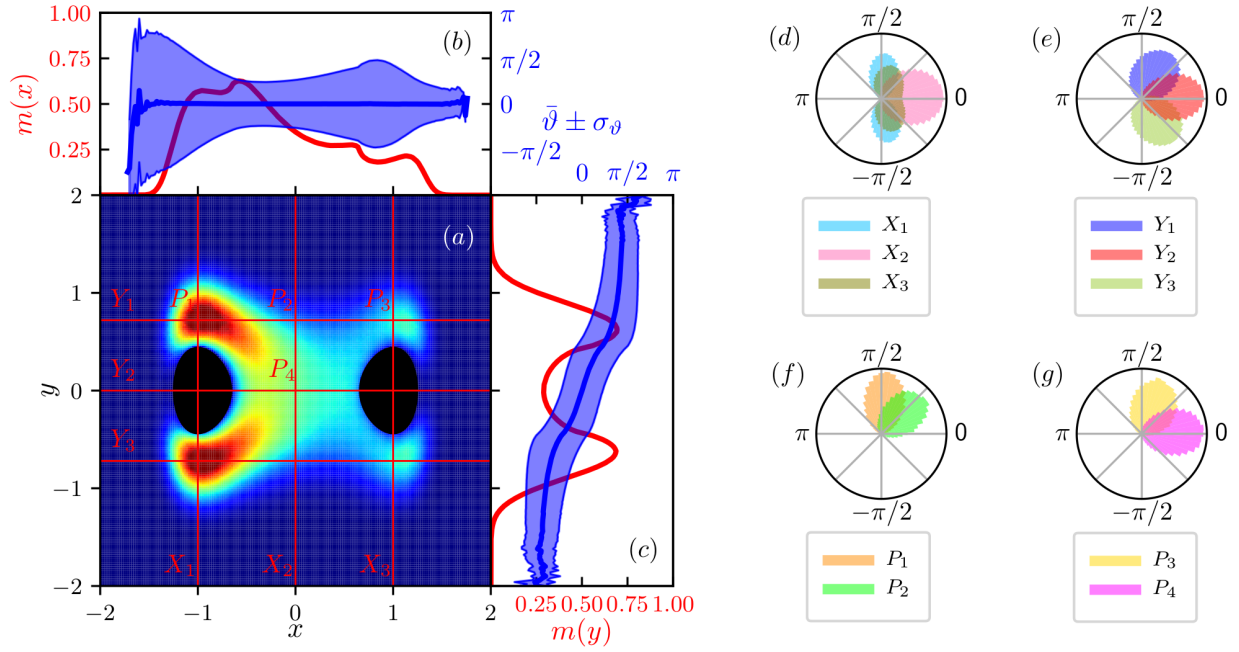


FIG. S4. (a) Reactive probability density $m(\mathbf{r})$ for $Pe = 5, k_x = 6, k_y = 20$. (b-c) marginal reactive probability density $m(x)$ ($m(y)$) (red line) and average angle $\bar{\vartheta}$ with its standard deviation σ_{ϑ} (thick blue line) as a function of x (y) alone. (d-e) distribution of angle ϑ among the states having x-coordinate in the intervals $X_1 : [-1 - \Delta, -1 + \Delta]$, $X_2 : [-\Delta, \Delta]$ and $X_3 : [1 - \Delta, 1 + \Delta]$ ($Y_1 : [-0.72 - \Delta, -0.72 + \Delta]$, $Y_2 : [-\Delta, \Delta]$ and $Y_3 : [0.72 - \Delta, 0.72 + \Delta]$) respectively ($\Delta = 0.04$). (f-g) distribution of angle ϑ in the states P_1, \dots, P_4 , at the intersection of previously defined intervals. Each angular distribution is normalized.

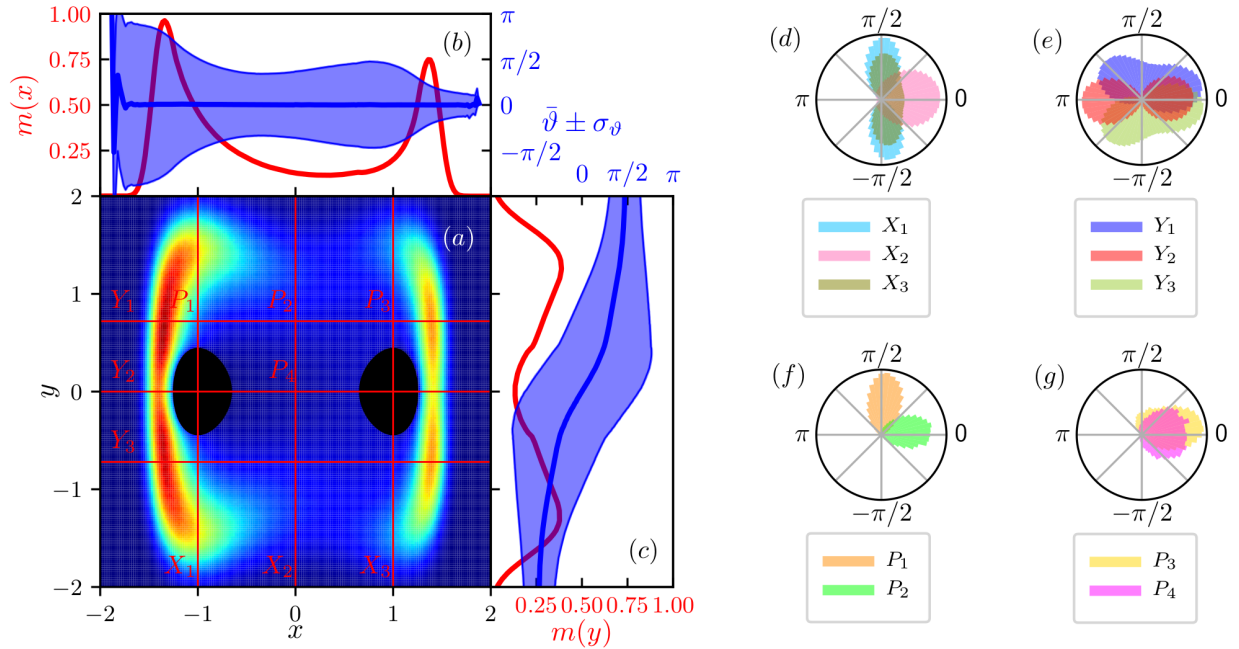


FIG. S5. (a) Reactive probability density $m(\mathbf{r})$ for $Pe = 10, k_x = 6, k_y = 20$. (b-c) marginal reactive probability density $m(x)$ ($m(y)$) (red line) and average angle $\bar{\vartheta}$ with its standard deviation σ_{ϑ} (thick blue line) as a function of x (y) alone. (d-e) distribution of angle ϑ among the states having x-coordinate in the intervals $X_1 : [-1 - \Delta, -1 + \Delta]$, $X_2 : [-\Delta, \Delta]$ and $X_3 : [1 - \Delta, 1 + \Delta]$ ($Y_1 : [-0.72 - \Delta, -0.72 + \Delta]$, $Y_2 : [-\Delta, \Delta]$ and $Y_3 : [0.72 - \Delta, 0.72 + \Delta]$) respectively ($\Delta = 0.04$). (f-g) distribution of angle ϑ in the states P_1, \dots, P_4 at the intersection of previously defined intervals. Each angular distribution is normalized.

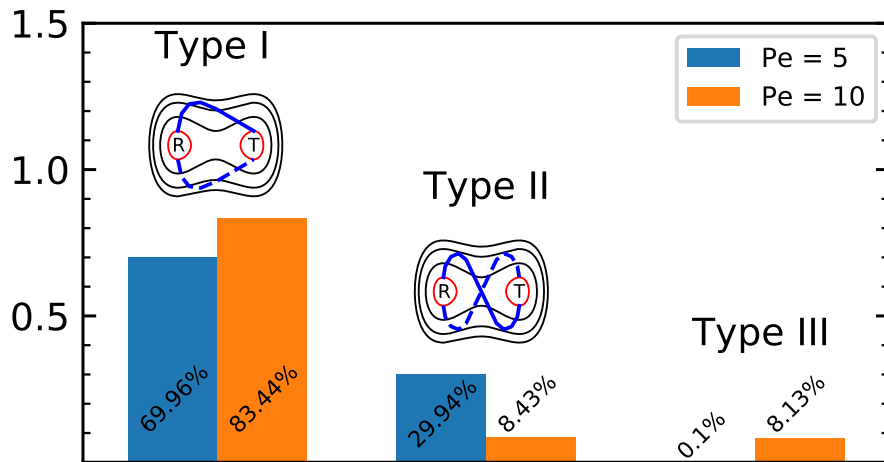


FIG. S6. Frequency of different trajectory types for two values of the Péclet number, $Pe = 5$ and $Pe = 10$. A sketch of the trajectory type is given above the bars.

trajectories are of type I, a relevant part is of type II while almost no other types of trajectories are observed. For $Pe = 10$, instead, the percentage of trajectories of the first kind increases as well as other possible types of trajectories, while the second type of trajectories decreases. The higher (lower) fraction of transition paths belonging to type I (II) for $Pe = 10$, in comparison to $Pe = 5$, is due to the fact that particles with higher activity are more likely to “surf” along the potential energy walls.

DEPENDENCE ON THE ENERGY LANDSCAPE

In this section we provide additional information on the target search patterns displayed by ABP in different energy landscapes.

First, we consider the same form of energy landscape discussed in the main text but with different potential stiffnesses. Fig. S7 shows the the transition path density, $m(\mathbf{r})$, and the transition current, $\mathbf{J}(\mathbf{r})$, for $Pe = 10$ when changing the stiffness parameter k_x . The variation in the quartic part of the potential is not introducing substantial changes in the reactive probability densities and currents, rather they remain quite similar for all explored values of k_x . The most notable difference resides again in the region explored by the active particles, that is getting closer to the basins along the x direction upon increasing the potential stiffness k_x .

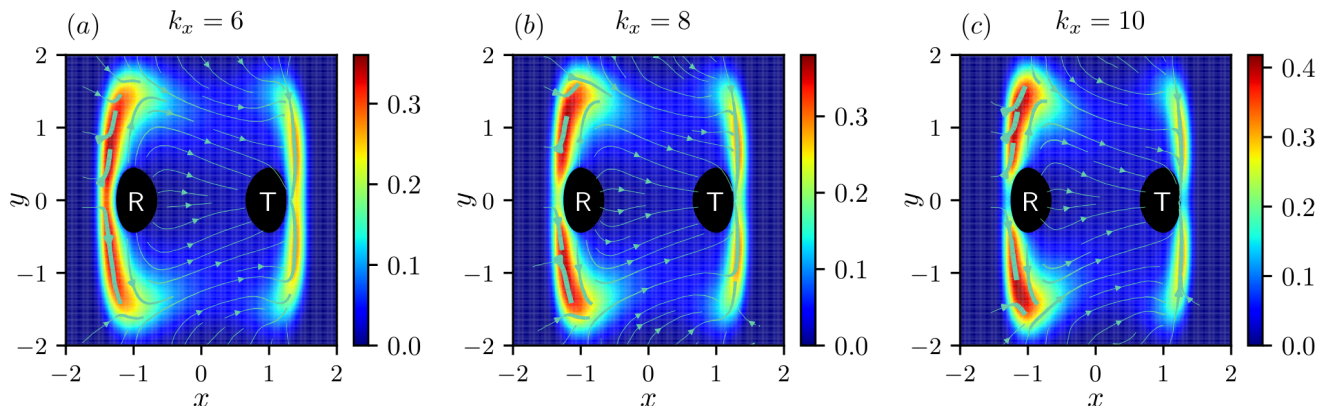


FIG. S7. (a-c) $m(\mathbf{r})$ and $\mathbf{J}(\mathbf{r})$ in the reactive region for $Pe = 10$ at different potential stiffnesses k_x with $k_y = 20$ (ABP parameters: $D = 0.1$, $D_\theta = 1$, $\mu = 0.1$, $v = 3.65$).

Then, we study the target-search scenario in a completely different energy landscape. We propose a Müller-like

potential of the form:

$$U(x, y) = \sum_{i=1}^3 K_i e^{[a_i(x-x_{0,i})^2 + b_i(x-x_{0,i})(y-y_{0,i}) + c_i(y-y_{0,i})^2]}, \quad (\text{S13})$$

with parameters

i	K_i	a_i	b_i	c_i	x_0^i	y_0^i
1	-10	-0.8	0	-5	1.7	0
2	-10	-3	6	-5	0.5	2
3	1	0.7	0.6	0.7	0	1

Given this energy landscape, we define the reactant basin (R) as the region with energy lower than $-2.5k_B T_{\text{eff}}$ around the minimum close to $(x_{0,1}, y_{0,1})$ (see inset in Fig. S8a). R is about $3.4k_B T_{\text{eff}}$ deep. The target basin is defined as the region with energy lower than $-4.7k_B T_{\text{eff}}$ around the minimum close to $(x_{0,2}, y_{0,2})$. T is about $2.7k_B T_{\text{eff}}$ deep. The saddle point separating R from T corresponds to an energy of about $0.9k_B T_{\text{eff}}$. In contrast to the energy landscape proposed in the main text, this one is highly asymmetric with a curved minimum energy path from R to T. Also in this case, the TPT distribution obtained using our TPS algorithm reproduces well the one obtained by direct integration of the stochastic equations of motion for all different considered values of the Péclet number (see Fig. S8a). Furthermore, increasing the activity the mode (i.e. the most likely transition path time) of the distribution shifts to shorter times while its right tail becomes longer, meaning that there are more very fast transition paths (see Fig. S8b) and, at the same time, an increase in the number of transition paths that take longer detour “surfing” high-energy regions before landing in the target region (see Fig. S8c). This mechanism is confirmed by an analysis of the transition-path density and of the transition current (see Fig. S8d for the case $Pe = 5$).

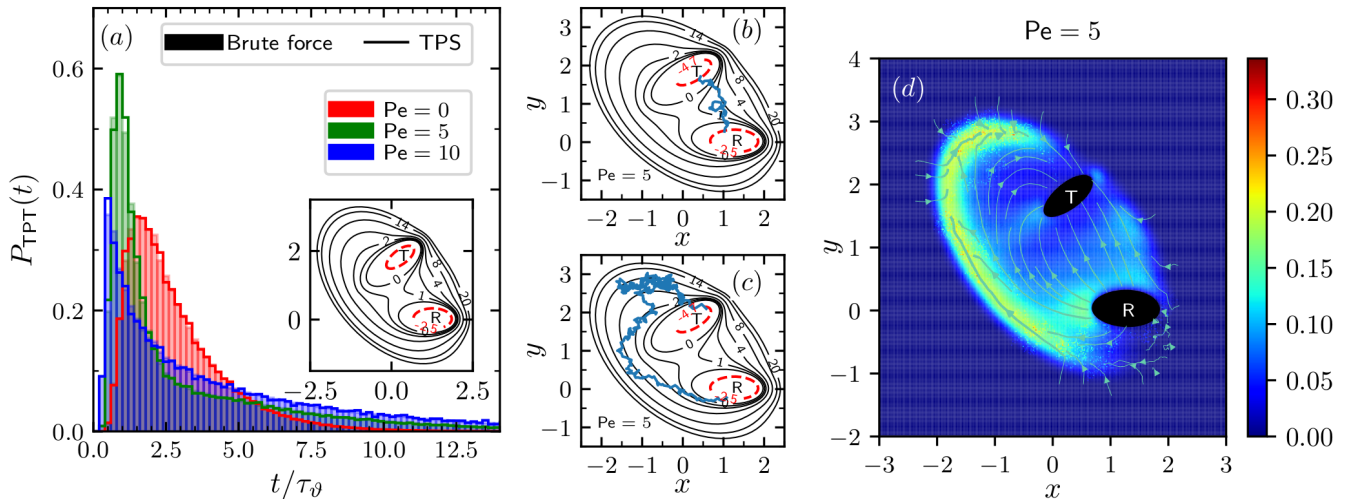


FIG. S8. (a) Distribution of TPTs at different Péclet numbers in the energy landscape reported in the inset. Each distribution is obtained from 10^6 different TPTs. (b) typical fast reactive paths at $Pe = 5$. (c) typical long reactive paths at $Pe = 5$. (d) Reactive probability density $m(\mathbf{r})$ (color map) and field lines of the reactive current $\mathbf{J}(\mathbf{r})$ (cyan arrows) at $Pe = 5$.

To conclude this section, we note that for the ABPs, the proposed TPS scheme can deal not only with the proposed paradigmatic potential energy surface but with virtually any landscape as long as well-defined reactant and target regions exist. In particular, in complex energy landscapes, one might be interested in how many typical reaction channels exist and on which transition states or metastable states are visited by the system on its way to the target. Practically, it is precisely the presence of many local minima that may pose severe issues to the efficiency of the TPS algorithm. To solve this problem classic TPS was complemented with a quenching technique [S4] and the same method can be applied and tested in our case.

DEPENDENCE ON THE ROTATIONAL DIFFUSION PARAMETER

In this section we study the ABP behavior for three different values of the Péclet number, $Pe := v\sqrt{3/4DD_\vartheta}$ obtained by keeping fixed the velocity $v = 1.83$ (corresponding to $Pe = 5$ in the main text) and changing the rotational diffusion parameter: $Pe = 3.5$ ($D_\vartheta = 2$), $Pe = 7.1$ ($D_\vartheta = 0.5$), and $Pe = 10$ ($D_\vartheta = 0.25$). Similarly to what happens when increasing the Péclet number by increasing the self-propulsion velocity v , the average TPT grows with the Péclet number and the TPT distribution becomes broader with more and more long-lasting trajectories (see Fig. S9). However, an interesting new feature emerges. Namely, at a low rotational diffusivity the TPT distribution becomes bimodal (see Fig. S9 for $Pe = 10$). This bimodality shows that, an increase in the Péclet number obtained by decreasing the rotational diffusion rather than by increasing the velocity results in a more clear separation between short reactive paths traveling close to the minimum-energy path and long-lasting trajectories in which the particles “surf” along the energy walls before landing into the target. The plots of the reactive probability density and the transition current further underline the differences of the ABP behavior when the same Péclet number is obtained through different sets of the parameters v and D_ϑ (see Fig. S10). For example, a comparison of Fig. 3c ($v = 3.65$, $D_\vartheta = 1$) and Fig. S10c ($v = 1.83$, $D_\vartheta = 0.25$), both corresponding to $Pe = 10$, shows that when the velocity is higher the transition-path density is larger in the region behind the basins while when the rotational diffusivity is higher the transition path density is larger in the regions below and above the basins.

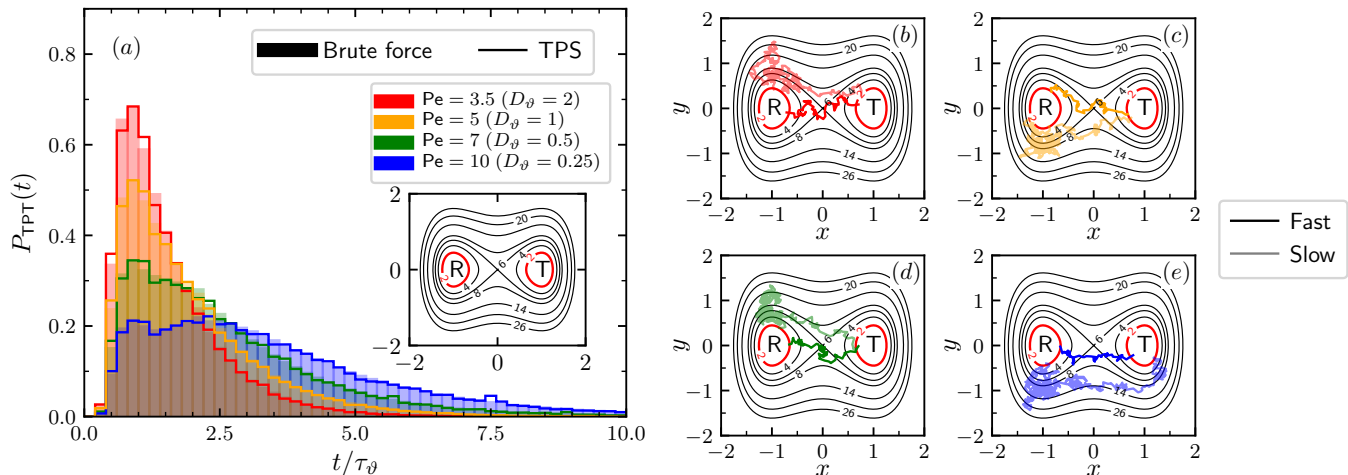


FIG. S9. (a) Distribution of Transition-path times (TPTs) at different Péclet numbers obtained by changing the rotational diffusion coefficient. Each distribution is obtained from 10^6 different TPTs. (b-e) A fast and a slow reactive path for each Péclet number considered in panel a. Color code as in panel a. (ABP parameters: $D = 0.1$, $\mu = 0.1$, $v = 1.83$. Potential parameters: $k_x = 6$, $k_y = 20$).

Similarly to what has been done in Section IV, different transition pathway are sorted in the three categories (see Fig. S11). Again most of the trajectories are of type I with a relative frequency growing with the Péclet number. Type II trajectories are the second most abundant type at each Péclet number considered and very few other types of trajectories are observed. Interestingly enough, a comparison with Fig. S6 shows that at fixed Péclet number, $Pe = 10$, type III trajectories are more frequent for the parameters set ($v = 3.65$, $D_\vartheta = 1$) than for ($v = 1.83$, $D_\vartheta = 0.25$).

BEHAVIOR FOR STRICTLY CONFINING POTENTIAL AT $D = 0$

Up to now, in our study the self-propulsion velocity v is always such that the barrier can be crossed even without the translational diffusion term. However, similarly to what is done in Ref. [S5], it is also interesting to consider another regime, namely the case in which the potential is a strictly confining potential in the limit $D \rightarrow 0$, i.e. the barrier cannot be crossed in the absence of fluctuations.

Assuming the potential landscape discussed in the main text and keeping fixed all others parameters, the maximum value of v for which the potential is strictly confining at $D = 0$ is $v = 0.9$, corresponding to a Péclet number $Pe = 2.46$. A plot of the reactive probability density and of the reactive current, shows that for such a low activity the behavior of the ABP is very similar to the behavior of a passive particle, i.e. its transition pathways travel close to the minimum

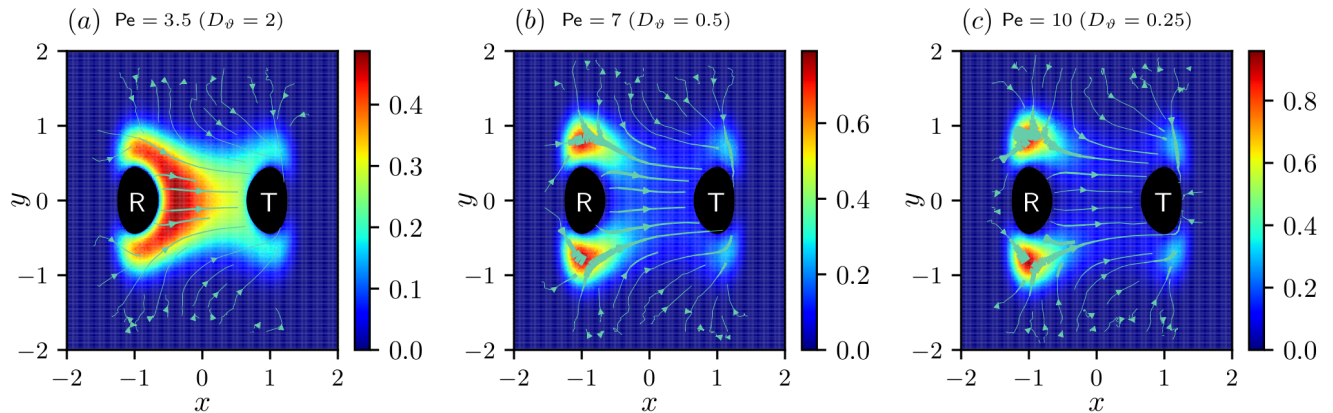


FIG. S10. (a-c) $m(\mathbf{r})$ and $\mathbf{J}(\mathbf{r})$ in the reactive region for different Péclet number obtained by changing D_θ (ABP parameters: $D = 0.1$, $v = 1.83$, $\mu = 0.1$. Potential parameters: $k_x = 6$, $k_y = 20$).

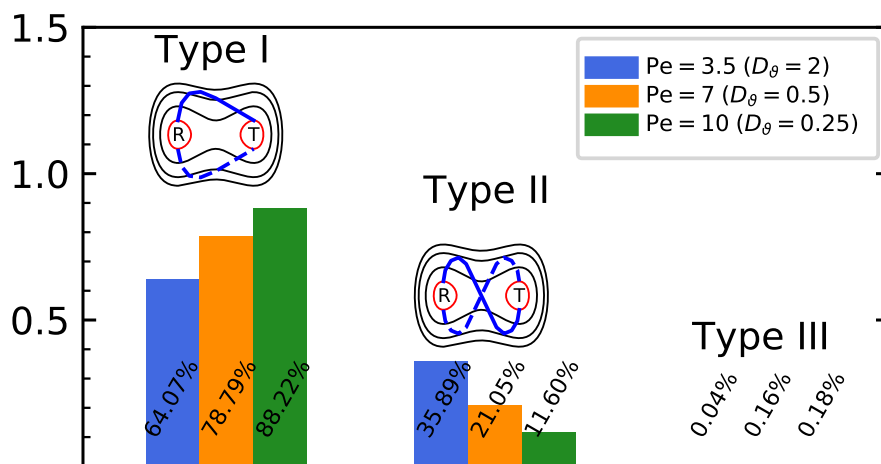


FIG. S11. Frequency of different trajectory types for three values of the Péclet number obtained by changing D_θ . A sketch of the trajectory type is given above the bars (ABP parameters: $D = 0.1$, $v = 1.83$, $\mu = 0.1$. Potential parameters: $k_x = 6$, $k_y = 20$).

free energy path without the long detours typical of more active particles (see Fig. S12a). Alternatively, one can consider a higher activity and make the potential strictly confining potentials at $D = 0$ by increasing the stiffness parameter k_x . For the case of $Pe = 5$ ($v = 1.83$) considered in the main text this condition is obtained for $k_x = 12$. In this case, one can notice that, while the reactive paths of the ABP tend to go through the saddle point of the energy landscape (in $x = 0$, $y = 0$), the way they exit the reactant basin is very different from the passive case (see Fig. S12b).

CROSSING RATES FROM REACTANT BASIN TO TARGET BASIN

Table reports the crossing rates from reactant basin to target basin in the various potential and parameter setups we have considered in our study. Even if in principle it is possible to obtain information on rates in the TPS framework complemented with transition interface sampling[S6, S7], at this stage we obtained the crossing rates directly from brute force simulations. From the Table it is possible to see how, for the parameter sets considered, the rates of active particles are always about two orders of magnitude higher than those of passive particles. However, considering ABPs only, the dependence of rates on the parameters is less clear. For example, the crossing rate grows with the Péclet number if the latter increases because of a change in the self-propulsion velocity, but it decreases if the increase in the Péclet number is due to a lower rotational diffusion coefficient. We expect that the target-search process is optimized for some particular set of parameters and that this set depends on the particular energy landscape under

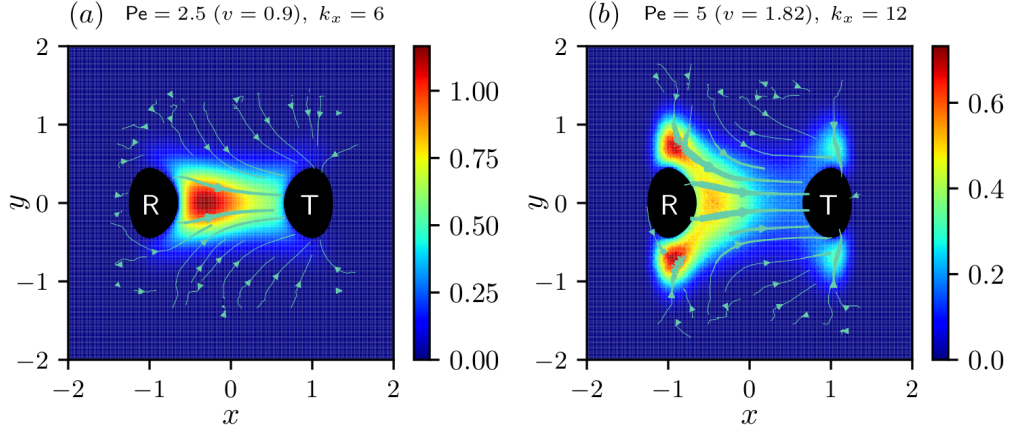


FIG. S12. $m(\mathbf{r})$ and $\mathbf{J}(\mathbf{r})$ in the reactive region for the parameters reported above the panels. (Fixed parameters: $k_y = 20$, $D = 0.1$, $D_\vartheta = 1$, $\mu = 0.1$).

	Pe = 0 ($D_\vartheta=1$, $v=0$)	Pe = 3.5 ($D_\vartheta=2$, $v=1.83$)	Pe = 5 ($D_\vartheta=1$, $v=1.83$)	Pe = 7 ($D_\vartheta=0.5$, $v=1.83$)	Pe = 10 ($D_\vartheta=0.25$, $v=1.83$)	Pe = 10 ($D_\vartheta=1$, $v=3.65$)
double well ($k_x=6$, $k_y=20$)	$6.32 \cdot 10^{-4}$	$5.61 \cdot 10^{-2}$	$5.63 \cdot 10^{-2}$	$4.46 \cdot 10^{-2}$	$2.93 \cdot 10^{-2}$	$5.62 \cdot 10^{-2}$
double well ($k_x=8$, $k_y=20$)	$1.15 \cdot 10^{-4}$	$4.15 \cdot 10^{-2}$	$4.6 \cdot 10^{-2}$	$3.92 \cdot 10^{-2}$	$2.7 \cdot 10^{-2}$	$6.07 \cdot 10^{-2}$
double well ($k_x=10$, $k_y=20$)	$1.93 \cdot 10^{-5}$	$2.59 \cdot 10^{-2}$	$3.25 \cdot 10^{-2}$	$3.1 \cdot 10^{-2}$	$2.31 \cdot 10^{-2}$	$6.25 \cdot 10^{-2}$
Müller-like potential	$2.61 \cdot 10^{-4}$	$3.99 \cdot 10^{-2}$	$3.94 \cdot 10^{-2}$	$3.05 \cdot 10^{-2}$	$2.03 \cdot 10^{-2}$	$4.85 \cdot 10^{-2}$

TABLE I. Crossing rates from reactant basin to target basin. In all cases $D = 0.1$ and $\mu = 0.1$. Parameters of the Müller-like potential are reported in Section . Rates are in units of the inverse computational time.

considerations. In particular, one may be interested in finding the optimal set of parameters in a complex energy landscape with several low-lying minima.

* Thomas.Franosch@uibk.ac.at

† pietro.faccioli@unitn.it

[S1] L. Onsager and S. Machlup, *Phys. Rev.* **91**, 1505 (1953).

[S2] S. Machlup and L. Onsager, *Phys. Rev.* **91**, 1512 (1953).

[S3] S. Shankar and M. C. Marchetti, *Phys. Rev. E* **98**, 020604 (2018).

[S4] C. Dellago, P. G. Bolhuis, and D. Chandler, *J. Chem. Phys.* **108**, 9236 (1998).

[S5] E. Woillez, Y. Zhao, Y. Kafri, V. Lecomte, and J. Tailleur, *Phys. Rev. Lett.* **122**, 258001 (2019).

[S6] T. S. van Erp, D. Moroni, and P. G. Bolhuis, *J. Chem. Phys.* **118**, 7762 (2003).

[S7] T. S. van Erp and P. G. Bolhuis, *J. Comput. Phys.* **205**, 157 (2005).